Materials & Design 263 (2026) 115639

Contents lists available at ScienceDirect

Materials & Design

journal homepage: www.elsevier.com/locate/matdes

Geometry effect on titania nanoparticle distribution and its impact on the photocatalytic properties of vat photopolymerization 3D-printed acrylic resin-based nanocomposites

Libera Vitiello [a,*,1], Giuseppe Proietto Salanitri [b,1], Paolo Maria Riccobene [a], Maria Grazia Pia Musumeci [c], Roberto Fiorenza [c], Sabrina Carola Carroccio [a]

[a] CNR-IPCB Institute for Polymers, Composites and Biomaterials CNR-IPCB, Via Paolo Gaifami 18, Catania 95126, Italy
[b] Department of Industrial Chemistry "Toso Montanari", University of Bologna, Via Piero Gobetti 85, 40129 Bologna, Italy
[c] Department of Chemical Sciences, University of Catania, V.le A. Doria 6, Catania 95125, Italy

ARTICLE INFO

Keywords:
3D printing
Hybrid composites
Titania nanoparticles
Photocurable resin
Photocatalysis

ABSTRACT

The development of geometrically optimized photocatalytic devices is a key challenge for advancing environmental purification technologies. The incorporation of titanium dioxide (TiO_2) nanoparticles into polymeric materials, combined with additive manufacturing, offers a promising route to fabricate photocatalytic structures with custom-designed architectures. This paper investigates how specific geometric design influences nanoparticle distribution and its effect on the photocatalytic performance. A commercial acrylic resin was loaded with different TiO_2 concentrations (2.5, 5, 10 wt%), and optimal printing conditions were identified to achieve high-resolution structures. Characterization through cure depth measurements, ATR-FTIR spectroscopy, thermogravimetric analysis, scanning electron microscopy, and energy-dispersive X-ray spectroscopy confirmed effective photopolymerization and thermal stability, enabling evaluation of nanoparticle distribution in 3D-printed nanocomposites. Gyroid, lattice, and wheel geometries were designed to assess shape effects on titania distribution via photocatalytic testing. Topologically constrained and intralayer regions promote nanoparticle surface enrichment. Specifically, complex networks exhibit greater surface segregation than simple geometries, enhancing TiO_2 photoactivity. The gyroid, characterized by the highest number of layers, displayed the best photocatalytic activity, with a 43% increase in the reaction rate constant compared to the wheel geometry at 10 wt% TiO_2. These findings demonstrate that tailoring material formulation and geometry can maximize the performance of 3D-printed photocatalytic devices.

1. Introduction

Nanomaterials have attracted considerable attention in recent decades due to their distinctive chemical and physical properties, which differ markedly from those of their bulk counterparts [1–3]. At the nanoscale, the high surface-to-volume ratio enhances surface reactivity, making these materials highly attractive for a broad range of applications, including catalysis, energy storage, environmental remediation, and pollutant detection [4,5]. Among the different nanomaterials investigated, titanium dioxide (TiO_2), commonly known as titania, stands out for its excellent physicochemical characteristics such as high thermal stability, strong photocatalytic activity, chemical inertness, and relatively low production costs [6]. TiO_2 can be chemically activated by UV light irradiation, triggering surface photochemical reactions through the direct absorption of incident photons [7]. These properties make it an excellent candidate for applications in photocatalytic water and air purification, self-cleaning surfaces, antibacterial coatings, hydrogen production and storage, solar energy conversion, and sensor technologies [8,9]. Despite these outstanding functional properties, the practical deployment of TiO_2 nanoparticles in real-world systems remains challenging. Their nanoscale dimensions complicate recovery, reuse, and long-term stability, limiting scalability and industrial integration. A promising strategy to overcome these limitations involves embedding TiO_2 nanoparticles within macroscopic three-dimensional structures,

* Corresponding author.
E-mail address: libera.vitiello@cnr.it (L. Vitiello).
[1] These authors contributed equally.

https://doi.org/10.1016/j.matdes.2026.115639
Received 17 December 2025; Received in revised form 29 January 2026; Accepted 9 February 2026
Available online 11 February 2026

which facilitate handling and recovery while preserving catalytic efficiency and structural integrity [10–12].

Polymeric materials are ideal candidates for such structural integration. Thanks to their various chemical composition and adaptable morphological features, polymers provide a versatile matrix for integrating photocatalytic nanomaterials [13–15]. A wide range of fabrication techniques have been investigated for the development polymer–based nanocomposites, aiming to combine the functional properties of nanomaterials with the mechanical robustness and processability of polymers [16–18]. However, beyond the mere inclusion of nanoparticles in a polymer matrix, the architecture of the composite plays a crucial role. The geometry of the support structure significantly influences light penetration, photon absorption, and the accessibility of the photocatalytic active sites [19–21]. Therefore, optimizing structural design is essential for enhancing overall photocatalytic performance.

In this context, additive manufacturing (AM) has emerged as a cutting-edge technology for producing polymer-based nanocomposites with precise, complex, and customizable geometries [22,23]. Unlike traditional subtractive approaches, AM offers greater design flexibility, efficient material use, and rapid prototyping capabilities [24]. The integration of nanomaterials with AM enables the development of multiscale systems that retain the specific functionality of the nanomaterials while improving production efficiency through rapid prototyping, greater component integration, and reduced material waste [25–27]. Embedding TiO_2 nanoparticles into printable polymeric matrices allows for the fabrication of complex structures that preserve the photocatalytic capabilities of the nanoparticles while leveraging the scalability and dimensional control provided by 3D printing technologies [28].

Among the various AM techniques, vat photopolymerization, especially in its Liquid Crystal Display (LCD) variant, has proven especially effective. This method enables the production of high-resolution, low-porosity components with complex geometries, making it a promising approach for the fabrication of efficient photocatalytic systems [29–33]. Polymer nanocomposites processed by additive manufacturing have been widely explored using a variety of nanoparticles to impart enhanced or multifunctional properties. Different fillers, such as biochar, silicon nitride, zinc oxide, and graphene nanoplatelets, have been incorporated into polymeric resins to enhance mechanical, antibacterial, biocompatible, or multifunctional properties of the printed components [34–36]. In vat photopolymerization-based systems, particular attention has been devoted to optimizing filler content in order to maintain printability while improving bulk material performance. Similarly, 3D printed titania-based composites have been investigated primarily with respect to their physical, mechanical, and structural properties, often in combination with additional functional fillers [35,37]. While these studies clearly demonstrate the versatility of additive manufacturing for producing multifunctional nanocomposites, limited attention has been paid to how architectural design can actively influence nanoparticle surface segregation and functional performance, particularly in photocatalytic applications.

Addressing this gap, the present study aims to explore the tunability of complex 3D-printed polymer structures loaded with TiO_2 using LCD printing technology for photocatalytic applications. To figure out how geometries can influence nanoparticle distribution and its related photocatalytic performance, three architectures were selected: a triply periodic minimal surface (TPMS) gyroid, a spherical lattice, and a simple wheel, thereby emphasizing the active role of structural design (Scheme 1). This approach can contribute to the rational development of next-generation catalytic systems, where the 3D-printed support functions not as a passive scaffold but as an active structural feature that influences overall catalytic performance. The dispersion of TiO_2 nanoparticles in the photopolymer resin was optimized to achieve high-resolution printing formulations. As a preliminary and essential step toward the fabrication of TiO_2-based photocatalytic architectures by vat photopolymerization, the printability of resin formulations containing

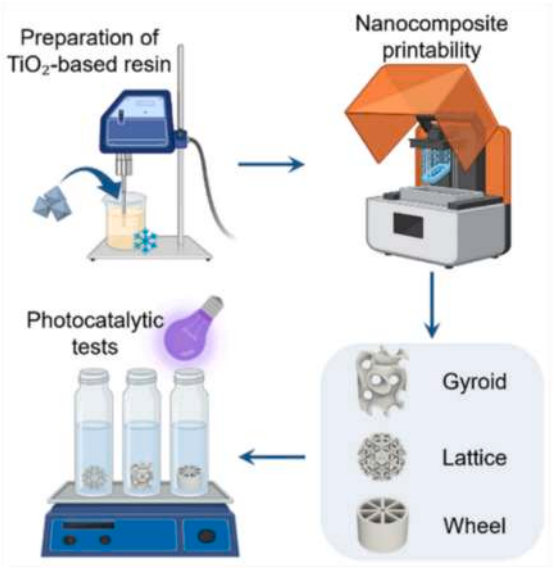

Scheme 1. Schematic workflow of the preparation and characterization of TiO_2-based photocurable nanocomposites: resin formulation and dispersion, LCD 3D printing of samples with different geometries (gyroid, lattice, and wheel), and assessment of their photocatalytic activity.

2.5, 5, and 10 wt% TiO_2 was systematically assessed. The morphology and distribution of TiO_2 loaded in the printed polymer structures were characterized using scanning electron microscopy (SEM) and energy-dispersive X-ray spectroscopy (EDX). Thermogravimetric analysis (TGA) was employed to assess thermal stability and determine the actual TiO_2 content in the polymer matrix. Finally, the photocatalytic performance of samples with different geometries and TiO_2 concentrations was evaluated under UV irradiation by monitoring the degradation of a model organic dye (methylene blue) in aqueous solution. The results demonstrate that, in addition to TiO_2 content, geometric complexity plays a key role in governing nanoparticle surface segregation. In particular, triply periodic minimal surface architectures exhibit the highest photocatalytic activity driven by enhanced nanoparticle enrichment.

2. Experimental section

2.1. Materials

A clear acrylic UV resin designed for LCD 3D printing was supplied by Phrozen Technology (Phrozen Aqua 3D Printer Resin), with viscosity: 50 – 100 cps, density of 1.11 g/cm^3 and tensile strength at break of 22 MPa. TiO_2 P25 Aeroxide (80% anatase, 20% rutile, 50 m2/g surface area, <100 nm of particle size) was used as purchased from Acros Organics.

2.2. TiO_2-based resin preparation

The TiO_2-loaded resin was prepared following a three-step process to optimize nanoparticle dispersion. First, titanium dioxide nanoparticles were sieved through an 80–140 mesh to remove large agglomerates. Then, they were added to the resin under mechanical stirring and mixed for 15 min to achieve uniform initial dispersion. Finally, the loaded resin was subjected to sonication using an ultrasonic homogenizer (UP200St, Hielscher; 200 W, 26 kHz) to further enhance dispersion. The sonication process was conducted in an ice bath, maintaining a temperature of approximately 15°C. Sonication lasted 15 min, alternating 2 s of activity with 2 s of rest, using a power of 30 W and an amplitude of 70%. The resin was prepared with TiO_2 concentrations of 2.5 wt%, 5 wt%, and 10

wt%. Dispersion stability was qualitatively assessed by observing sedimentation.

2.3. Evaluation of printing conditions

The printability of the TiO_2-based resin was evaluated through photopolymerization experiments using an LCD 3D printer, the Phrozen Sonic Mini 8 K (Phrozen Tech Co., LTD, Hsinchu, Taiwan). The photopolymerization depth of the dispersions, C_d, was measured at different exposure times, t_e, (ranging from 10 s to 100 s) by determining the thickness of the single cured layer with a micrometer. Each measurement was performed in triplicate to ensure reproducibility. To determine the optimal printing conditions for high dimensional accuracy, a test sample was designed. The 3D-printed model consisted of a flat square base topped with a raised square frame, featuring sides of 10 mm and a wall thickness of 0.5 mm, as illustrated in Fig. S1. Dimensional accuracy was assessed through microscopic measurements of three key parameters: the outer side lengths of the frame (l_o and l_v, respectively) and its thickness (t_w). Optimal printing conditions were defined as those that minimized deviations from the nominal dimensions. For each resin formulation, the test sample was printed at three different exposure times using default printing profiles optimized for the specific resin, unless otherwise specified. After printing, samples were cleaned by sonication in isopropanol and dried using compressed air to eliminate residual uncured resin. A post-curing step was then performed in a UV chamber for 10 min to complete polymerization.

2.4. Printed sample characterization

To verify the chemical composition of the materials and confirm the absence of unreacted monomers in the final composites, samples were characterized by Attenuated Total Reflectance Fourier Transform Infrared Spectroscopy (ATR-FTIR). Spectra were recorded within the 2400–540 cm^{-1} range using a Thermo Scientific™ Nicolet™ iS50 FTIR Spectrometer equipped with a Diamond DLaTGS detector. Each spectrum was acquired by averaging 32 scans at a resolution of 4 cm^{-1}. Thermogravimetric analysis (TGA) was performed using a Perkin Elmer TGA 8000 (Waltham, MA, USA) apparatus to assess the thermal stability and actual TiO_2 content of the printed samples. Approximately 8 mg of each sample was heated under a nitrogen flow (60 mL/min) from 50°C to 700°C, followed by heating under an air flow (60 mL/min) up to 800°C at a rate of 10°C/min. Morphological characterization of the printed samples was conducted using a Thermo Phenom ProX desktop SEM (Thermo Fisher Scientific, Waltham, MA, USA). Prior to analysis, the samples were coated with a gold layer thinner than 10 nm to enhance conductivity. The surface distribution of TiO_2 was examined using energy-dispersive X-ray spectroscopy.

2.5. Geometry design

Three distinct geometries, gyroid, lattice, and wheel, were designed to explore the impact of printing geometry on the nanoparticle distribution and the corresponding photocatalytic properties of the resulting nanocomposites. The structures were generated using Autodesk Netfabb (version 2025), maintaining a fixed nominal surface area of about 5.2 cm^2 and a wall thickness of 0.5 mm. These parameters were standardized to ensure comparability, as photocatalysis is a surface-driven process [38]. Further details on the three geometries are provided in the Supplementary Information (Fig. S2). Subsequently, the models were processed for 3D printing using Chitubox (Shenzhen, China), a professional slicing software. This step involved optimizing the orientation of the structures and integrating necessary supports to ensure optimal printability and structural integrity.

2.6. Photocatalytic tests

The photocatalytic activity of the 3D-printed nanocomposites with different geometries (gyroid, lattice, and wheel) was assessed through the degradation of methylene blue (MB), a widely used cationic organic dye that is a benchmark compound in photocatalysis research under UV irradiation [39]. For each geometry, three samples were immersed in a vial containing 20 mL of MB aqueous solution at an initial concentration of 5 ppm. Before UV exposure, the samples were kept in the dark until saturation to allow adsorption–desorption equilibrium to be reached, thus ensuring that subsequent dye removal was attributable to photocatalytic activity rather than simple adsorption. Photocatalytic experiments were conducted under continuous stirring using a platform shaker operating at 100 rpm to maintain homogeneous agitation of the dye solution. UV irradiation was provided by a UV-A lamp with a wavelength of 395 nm and a power of 40 W, with the vials positioned 15 cm from the light source. MB degradation was monitored at predefined time intervals using a UV–Vis V-750 spectrophotometer (Jasco Inc., Easton, MD, USA). The measurements were taken across the 800–400 nm range, with the primary focus on the dye's characteristic absorption peak at 664 nm. Dye concentration was quantitatively analysed using the Lambert–Beer law. To validate the photocatalytic activity of the TiO_2-based nanocomposites, control experiments were conducted on the MB aqueous solution under identical conditions but without samples. This baseline allowed for the isolation of the photocatalytic contribution of each sample by accounting for other potential degradation mechanisms, such as dye instability under UV irradiation.

3. Results and discussion

3.1. Printability

Photopolymerization experiments were conducted using LCD 3D printing to investigate the printability of both the unfilled resin and formulations containing different concentrations of TiO_2 nanoparticles. A preliminary assessment of dispersion stability was performed by monitoring sedimentation over time. After more than 48 h, no visible signs of TiO_2 sedimentation were observed, and all dispersions remained visually homogeneous (Fig. S3). To assess the photopolymerization behaviour of the different formulations, the photopolymerization depth, C_d, was measured as a function of UV exposure time, t_e, thereby modulating the total energy delivered to the system. As expected for photopolymerizable systems, C_d exhibited an exponential increase with increasing exposure time (Fig. 1a) [40,41]. The addition of TiO_2 nanoparticles significantly reduces the cure depth at any given exposure time. Moreover, the thickness of the cured layer decreases proportionally as the TiO_2 content increases, demonstrating a clear dependence of light penetration and polymerization efficiency on TiO_2 concentration. The photopolymerization kinetics are well described by a logarithmic relationship known as Jacobs' working curve, which relates the cure depth to the delivered energy according to the following expression (Eq. (1)) [42]:

$$C_d = D_p \ln \frac{E_a}{E_c} \tag{1}$$

where E_a is the energy per unit area delivered to the resin (calculated by multiplying the UV exposure time, t_e, by the power per unit area, 0.65 mW/cm^2, as measured on the printer screen), D_p represents the material's sensitivity to energy variations, and E_c is the critical energy required to start photopolymerization. Plotting C_d versus the logarithm of E_a yields a linear trend (Fig. 1b), from which the parameters D_p and E_c were derived for each formulation (Table 1). The results demonstrate that increasing the TiO_2 nanoparticles content significantly affects these parameters: D_p decreases, while E_c increases with higher nanoparticle loadings. This trend reflects a reduction in the photosensitivity of the

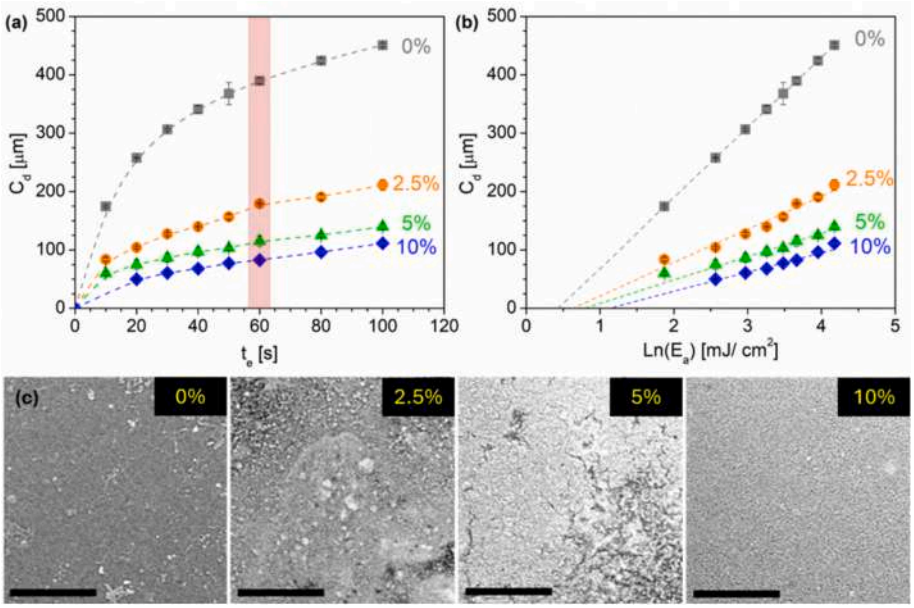

Fig. 1. Printability of TiO_2-filled resin at different concentrations. (a) Photopolymerization depth, C_d, as a function of UV exposure time, t_e, in LCD printing for pure resin and resin systems loaded with 2.5%, 5%, and 10% TiO_2; (b) dependence of photopolymerization depth on the energy density supplied to the material, E_a, of pure and TiO_2-loaded resin; (c) SEM images of the cured single layers at t_e = 60 s (scale bar 100 µm). The dashed lines are guides for the eye.

Table 1
Material sensitivity to a variation in supplied energy (D_p) and critical energy required to start the photopolymerization (E_c) of the resin loaded with different TiO_2 contents.

TiO_2 [wt.%]	D_p [µm]	E_c [mW/cm^2]
0	120	1.5
2.5	57	1.8
5	40	2.2
10	33	3.0

resin formulations. These findings corroborate the results obtained from direct measurements of cure depth. At an exposure time of 60 s, C_d decreases by 54% for the 2.5% TiO_2 formulation, 70% for 5%, and 79% for 10%, compared to the unfilled resin (see red box in Fig. 1a). This progressive reduction in cure depth is attributed to the optical properties of TiO_2 nanoparticles, which strongly absorb and scatter UV light [43]. Owing to their strong absorption in the UV-A and UV-B regions (280–400 nm), consistent with a wide bandgap of around 3.2 eV [44], TiO_2 particles act as competing absorbers, limiting the amount of UV energy available to activate the photoinitiator. Therefore, a substantial portion of the incident light is attenuated before it can activate the photoreactive species within the resin matrix, reducing the overall efficiency of the photopolymerization process. The dispersion of TiO_2 nanoparticles within the different formulations was carefully evaluated using SEM analysis. In particular, comparing single layers obtained with and without sonication, demonstrating that the sonication step significantly reduces nanoparticle aggregation throughout the polymer matrix (see Fig. S4 in the Supplementary Information). SEM images of the cured layers after 60 s of UV exposure (Fig. 1c) confirm the increased presence of TiO_2 with higher loadings and reveal a generally good distribution of nanoparticles throughout the matrix. Despite the TiO_2-induced attenuation, all formulations achieve a sufficient cure depth to ensure compatibility with LCD-based 3D printing. These results suggest that although TiO_2 addition affects the kinetics and extent of polymerization, proper adjustment of exposure parameters can effectively mitigate these limitations, allowing for consistent and reliable printing performance even at high nanoparticle concentrations.

The reduction in photopolymerization depth caused by the incorporation of TiO_2 nanoparticles made it necessary to define specific exposure times, distinct from those optimized for the commercial neat resin. Identifying the optimal exposure time for each nanoparticle-loaded formulation is essential to ensure that the printed components accurately reproduce the shape and dimensions defined during the CAD design phase. To this end, a test specimen was designed (Fig. 2a) and printed using three different exposure times for each of the four formulations considered, i.e. the neat resin and its three TiO_2-based dispersions. The exposure times were selected to ensure the formation of single layers with a thickness of 50 µm, a value chosen to ensure high resolution and dimensional quality. These times were determined based on the experimental data correlating cure depth to UV exposure time (Fig. 1a). For each printed sample, three characteristic dimensions, namely the side lengths, l_o and l_v, and the frame thickness, t_w, were measured to evaluate the deviations from the nominal design dimensions. The results, shown in Fig. 2b-e, allowed identification of the exposure time that minimized dimensional variation (Δd) for each formulation. The analysis revealed that increasing the TiO_2 content requires a corresponding increase in exposure time to achieve dimensional accuracy. Specifically, the neat resin achieved the highest dimensional precision at an exposure time of 10.5 s, in accordance with the resin data sheet (Fig. 2b). The formulations containing 2.5% and 5% TiO_2 required 20 s (Fig. 2c, d), while the 10% TiO_2 formulation needed 30 s of exposure (Fig. 2e). These findings confirm the reduced photopolymerization efficiency induced by the TiO_2 nanoparticles and highlight the importance of carefully calibrating printing parameters, particularly exposure time, according to resin composition. Importantly, despite the longer exposure times required by nanoparticle-filled formulations, the optimized values remain within the range typically used for commercial resins in LCD-based 3D printing [45]. This ensures that all formulations remain compatible with standard processing times and equipment.

3.2. *Printed nanocomposite characterization*

The chemical nature of the resin employed was investigated through ATR-IR spectroscopy. Although the resin is a commercial formulation with undisclosed composition, some insights into its chemical structure were obtained by analyzing the pure resin before curing, the resin after 3D photopolymerization, and the corresponding composites containing

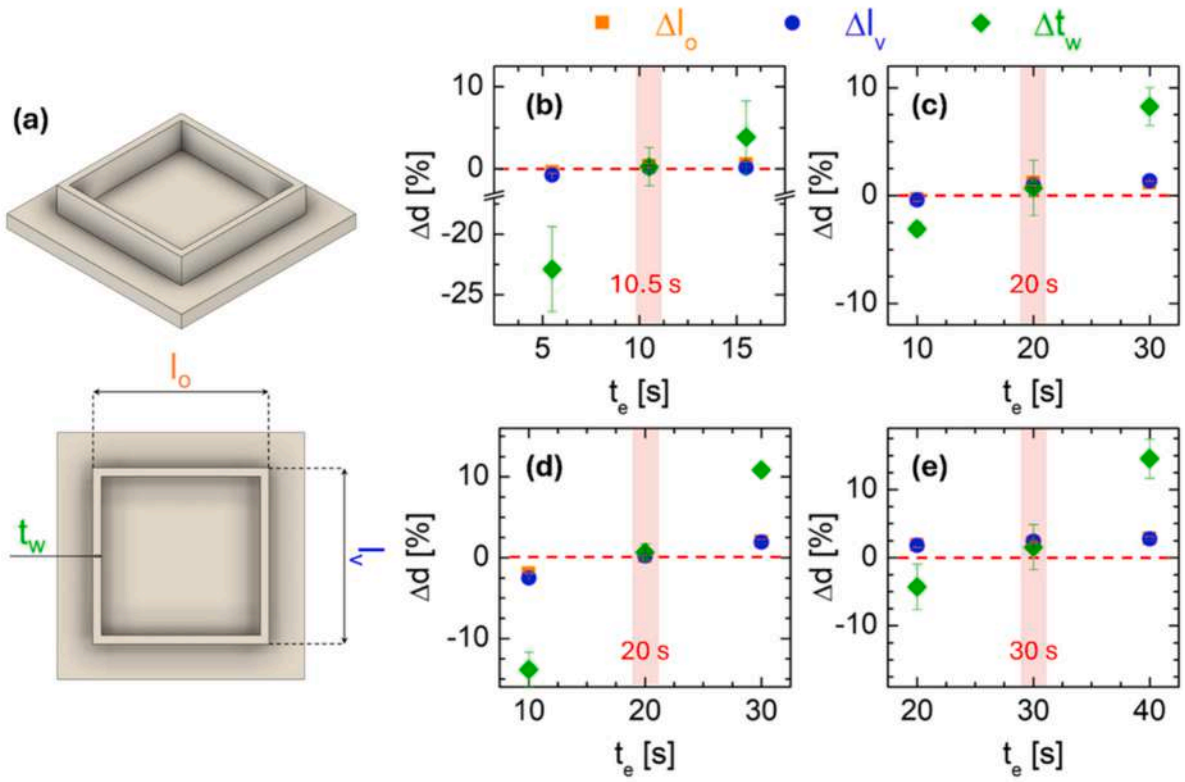

Fig. 2. Identification of optimal printing conditions. (a) Schematic representation of the 3D-printed model; dimensional variation, Δd, as a function of UV exposure time, t_e, in LCD printing for: pure resin (b) and resin loaded with 2.5% (c), 5% (d), and 10% (e) of TiO_2 nanoparticles.

2.5%, 5%, and 10% TiO_2 (Fig. 3a). In the unpolymerized resin, characteristic absorption bands associated with C=C stretching vibrations around 1620 cm^{-1}, as well as out-of-plane bending modes of mono- and disubstituted alkenes at approximately 910 and 790 cm^{-1}, were clearly observed. These peaks disappeared completely after photopolymerization (see red boxes in Fig. 3a), confirming the conversion of carbon–carbon double bonds during the curing process. This behavior is consistent with the typical reactivity of acrylate monomers [46] and indicates the effective crosslinking of the resin, with no detectable residual monomer, thus validating the reliability of the applied printing parameters. Notably, the same spectral evolution was observed for all TiO_2-loaded composites, demonstrating that the photopolymerization process remained effective even at the highest nanoparticle content. This result confirms that the selected UV exposure times were sufficiently optimized to ensure complete polymerization, despite the increased UV light absorption and scattering introduced by the TiO_2 filler. Additional relevant peaks include C–O stretching bands at 1110, 1190, 1240, and 1290 cm^{-1}, the C=O stretching vibration at 1720 cm^{-1} attributed to carboxylic acid, and the C=O stretch of amide (1640, 1680 cm^{-1}). In the spectra of the TiO_2-containing composites, a broad band appearing below ~ 750 cm^{-1} is observed, which can be attributed to the Ti–O stretching vibrations (see grey box in Fig. 3a) [47]. Thermal properties of the printed samples were assessed via thermogravimetric analysis under air atmosphere (Fig. 3b). The addition of TiO_2 nanoparticles did not lead to significant changes in the overall thermal stability of the pure printed resin. However, a notable enhancement in thermal stability was observed in the temperature at which a 5% weight loss occurs (T_5%). As reported in Supplementary Information Table S4, samples with 2.5% and 5% TiO_2 exhibited an increase in T_5% of approximately 28% relative to the pure resin. The thermal degradation profile displays two main weight-loss steps: the first between 300°C and 530°C, and the second from 560°C to 745°C. These steps are attributed to the degradation of the polymeric matrix, whose precise composition is not disclosed. At 800°C, the residual weight closely matches the theoretical filler content for each formulation: 0% for the neat resin, and approximately 2.7%, 5.3%, and 10.5% for the 2.5%, 5%, and 10% TiO_2 composites, respectively. These values confirm the successful and homogeneous incorporation of the inorganic filler. To investigate the surface morphology, SEM analysis was performed on the printed specimens. As shown in Fig. 3c, SEM images of the surface parallel to the printing direction reveal the characteristic stepwise architecture typical of LCD-based 3D printing, resulting from the layer-by-layer curing process [48]. Each layer exhibits a uniform thickness of 50 μm, in agreement with the defined printing parameters and consistent across all resin formulations. An increase in surface roughness was observed with increasing TiO_2 content. This effect is attributed to the progressive accumulation of nanoparticles on the surface. Since the photodegradation reactions triggered by TiO_2 occur at the material/water interface, this surface enrichment of nanoparticles is a positive outcome for the final application of such materials. EDX analysis further confirms the increase in surface TiO_2 concentration as the filler content of the uncured resin increases, with measured values exceeding the nominal nanoparticle loadings (Table S2). Moreover, EDX elemental mapping reveals a non-uniform distribution of the nanoparticles, with higher concentration detected in the interlayer regions (Fig. 3d). This suggests a tendency for TiO_2 nanoparticles to migrate toward the surface and accumulate at the interfaces during the layer curing [41,49], which could influence both the surface morphology and the photocatalytic behaviour of the final printed sample.

3.3. Geometry effect on photocatalytic properties

The photocatalytic activity of 3D printed TiO_2-based nanocomposites was measured to investigate the effect of printing geometries on nanoparticle distribution. Three distinct architectures, gyroid, lattice, and wheel (Fig. 4a) were designed. Each structure was printed

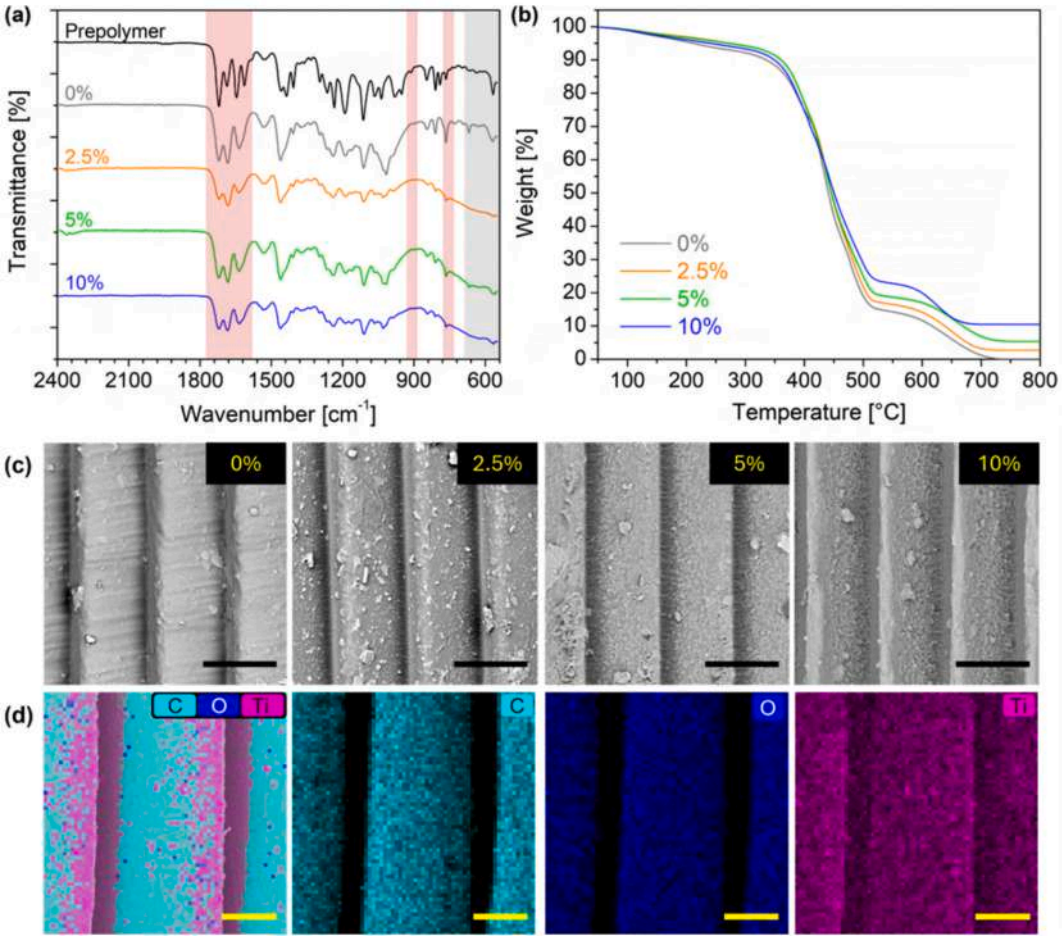

Fig. 3. Chemical, thermal and morphological properties of 3D printed nanocomposites. (a) ATR-IR profiles of the prepolymer and printed samples; (b) TGA thermograms of 3D-printed model sample loaded with different TiO_2 contents; (c) SEM images related to the surface morphology of the model samples (scale bar 50 μm); (d) EDX elemental mapping for data for C, O and Ti in 3D-printed model sample loaded with 10% TiO_2 (scale bar 30 μm).

using resin formulations containing 2.5 wt%, 5 wt%, and 10 wt% TiO_2 nanoparticles. Given that photocatalysis is a surface-dominated phenomenon, all geometries were designed to have a consistent nominal surface area of 5.2 cm^2 and a uniform wall thickness of 0.5 mm. This approach ensured that differences in photocatalytic activity could be attributed primarily to geometry and TiO_2 surface enrichment, rather than to variations in surface area. All formulations were printed using the baseline process parameters recommended for the specific commercial resin (Table S3), ensuring reliable and reproducible printing conditions. The only variable parameter was the UV exposure time, which was individually optimized for each TiO_2 loading based on the printability and curing behaviour determined in Section 3.1 (Fig. 1). This optimization was essential to compensate for the increased light absorption and scattering phenomena induced by the nanoparticles. Furthermore, all specimens were 3D printed with a 45° tilt angle and positioned 5 mm above the build platform, supported by light scaffolding structures. This inclination was selected based on preliminary printing tests, which showed that 45° orientation enhances excess resin drainage, thereby improving the resolution of the printed structures. Under these conditions, the number of layers required for complete fabrication depends on the geometry: 242, 185 and 171 layers for the gyroid, wheel, and lattice, respectively. SEM images of the three geometries containing 2.5% TiO_2 are presented in Fig. 4b, highlighting their distinct architectures. Detailed dimensional parameters for each structure are available in the Supporting Information (Fig. S2). SEM analysis confirmed the successful fabrication of the specimens and revealed different surface textures, which are critical for evaluating photocatalytic performance.

The photocatalytic performance of the 3D-printed TiO_2-based nanocomposites was evaluated by monitoring the UV-induced degradation of methylene blue (MB), selected as a model organic pollutant. The photocatalytic degradation mechanism of methylene blue in the presence of TiO_2 under UV irradiation, schematically illustrated in Fig. 5a, is governed by the generation of electron–hole pairs upon photoexcitation of the semiconductor. When TiO_2 absorbs photons with energy equal to or greater than its bandgap, electrons are promoted from the valence band to the conduction band, leaving positively charged holes in the valence band. These charge carriers can migrate to the TiO_2 surface, where they participate in redox reactions with adsorbed species. Photogenerated holes oxidize surface-bound water molecules or hydroxyl ions, leading to the formation of highly reactive hydroxyl radicals ($^{\bullet}OH$), while electrons reduce dissolved oxygen to generate superoxide radicals ($^{\bullet}O_2^-$). These reactive oxygen species act as the main oxidative agents responsible for the stepwise degradation of methylene blue molecules adsorbed at the TiO_2–solution interface, ultimately leading to their mineralization into smaller, less harmful species such as CO_2 and H_2O. Before exposure, all samples were kept in the dark to reach adsorption–desorption equilibrium, ensuring that subsequent changes in MB concentration were solely due to photocatalytic activity (Fig. S5). The degradation process was monitored using UV–Vis spectrophotometry, by measuring the variation in intensity of the characteristic MB absorption peak at 664 nm. Spectra were collected at regular time intervals to follow the temporal evolution of the photocatalytic degradation. MB concentrations were calculated from absorbance values using

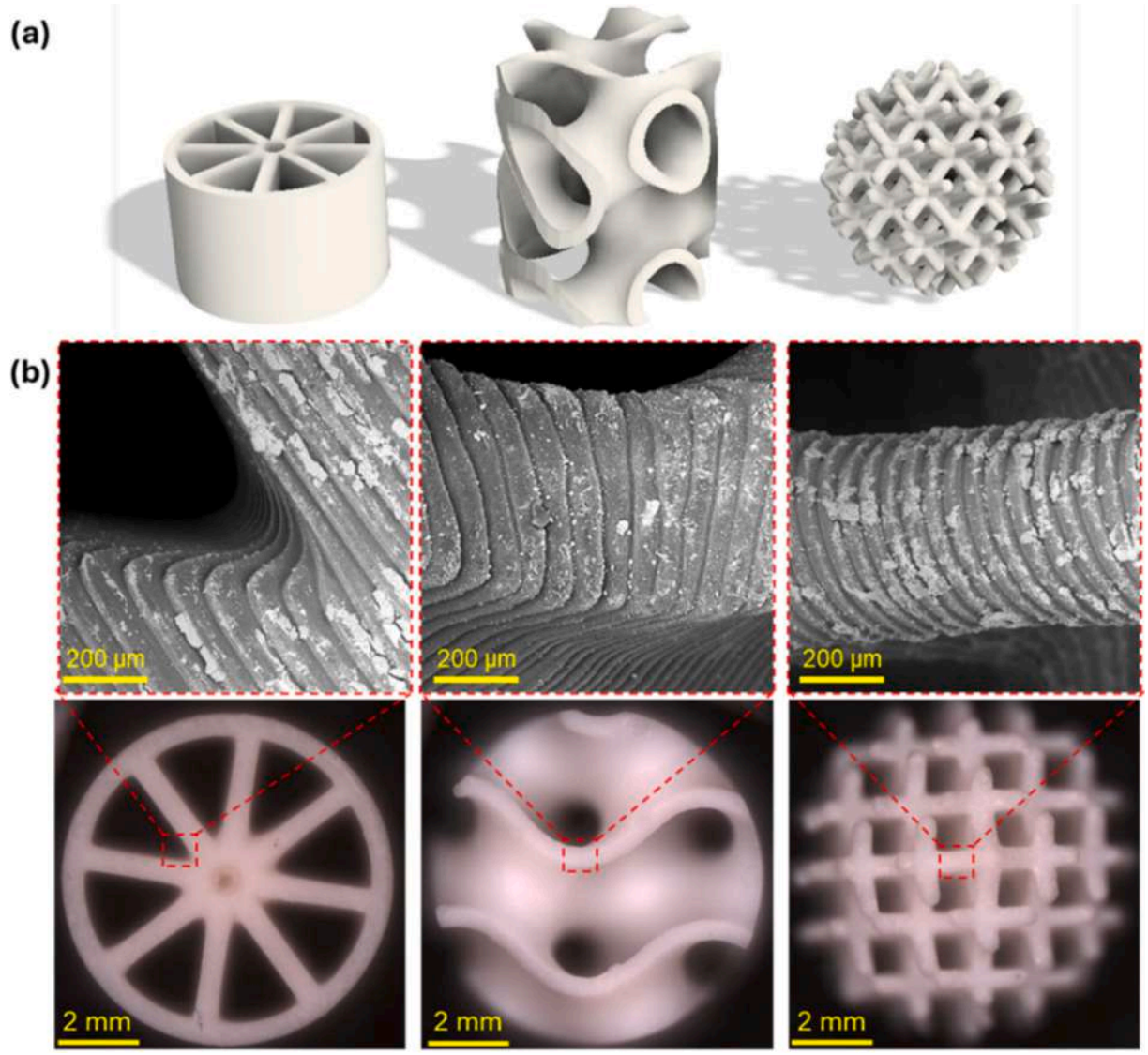

Fig. 4. Morphology of the three different geometries. (a) different three-dimensional macroscopic structures: wheel, gyroid, and lattice; (b) SEM images of the surface morphology of the three macrostructures loaded with 2.5% TiO_2.

the Lambert–Beer law, enabling a quantitative evaluation of photocatalytic efficiency. Fig. 5b shows the time-dependent decrease in MB concentration under UV exposure for the gyroid geometry at different TiO_2 contents. Comparable degradation trends were observed for the lattice sphere and wheel geometries, and their datasets are available in the Supplementary Information (Fig. S6). To validate the intrinsic photocatalytic activity of the TiO_2-based nanocomposites, control experiments were carried out using MB aqueous solutions without any printed samples under identical UV irradiation conditions. This baseline correction accounted for non-catalytic degradation pathways, such as MB photolysis and other non-catalytic degradation pathways, thereby allowing accurate quantification of the net photocatalytic contribution of each composite. All data were corrected accordingly. As expected, increasing the TiO_2 nanoparticle content led to a marked enhancement in photocatalytic activity across all geometries. Assuming pseudo-first-order kinetics, which typically describe the early stages of dye degradation [50], the reaction rate constant (k) was calculated using the following expression (Eq. (2):

$$\ln\left(\frac{C_0}{C}\right) = kt \tag{2}$$

where C_0 is the initial dye concentration, C is the concentration at time t, and k is the rate constant. The linear fit of the experimental data for the gyroid samples is shown in Fig. 5c, while analogous plots for the other geometries are provided in the Supplementary Information (Fig. S6). The calculated rate constants for all samples were then plotted as a function of TiO_2 content (Fig. 5d). A linear increase in the rate constant (k) was observed with increasing nanoparticle loading, confirming the positive correlation between filler content and photocatalytic efficiency. Importantly, the photocatalytic performance was also significantly influenced by geometry. Among the tested structures, the gyroid geometry demonstrated the highest photocatalytic efficiency, followed by the lattice, while the wheel geometry showed the lowest activity. These findings underscore the dual role of material composition and structural design in governing photocatalytic behaviour. While TiO_2 concentration is a dominant factor, the geometry of the printed component directly impacts active surface area.

To better understand how printing geometry affects the photocatalytic performance of TiO_2-based nanocomposites, SEM-EDX analyses were conducted to investigate the spatial distribution of TiO_2 both on the surface and within the printed samples (Fig. 6). The EDX elemental mapping of the cross-section of the wheel sample containing

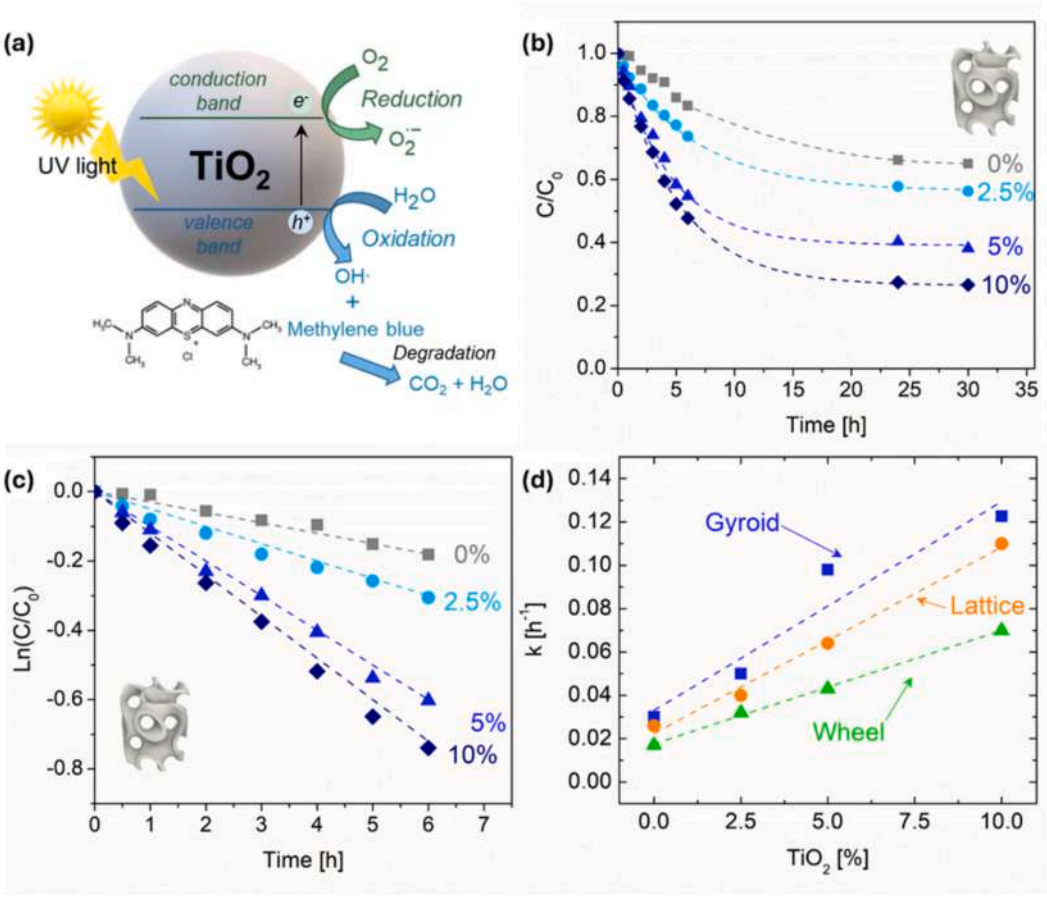

Fig. 5. Photocatalytic performance of 3D printed nanocomposites. (a) Photocatalytic degradation mechanism of methylene blue in the presence of TiO_2 under UV irradiation; (b) photocatalytic degradation of methylene blue over time from the gyroidal samples with 0%, 2.5%, 5% and 10% of TiO_2; (c) linear fit of the concentration variation during the first 6 h of testing for the gyroid samples; (d) rate constant variation in the photocatalytic reaction relative TiO_2 content for gyroid, lattice, and wheel samples. The dashed lines are guides for the eye. (For interpretation of the references to colour in this figure legend, the reader is referred to the web version of this article.)

10% TiO_2 reveals a pronounced enrichment of nanoparticles on the outer surface of the sample (Fig. 6a). This indicates a tendency for nanoparticles to migrate toward the outermost regions of each printed layer during fabrication, likely driven by segregation phenomena arising from flow dynamics and curing kinetics in the layer-by-layer printing process. To assess how geometry influences the distribution of TiO_2, SEM imaging coupled with EDX mapping was performed on different zones of the three distinct printed architectures (Fig. 6b–d). Across all geometries, TiO_2 was found to preferentially accumulate in intralayer regions (Fig. 6b′–d′), consistent with observations made on earlier test samples (Fig. 3d). This intralayer enrichment likely enhances photocatalytic efficiency, as these regions represent high-density interfacial areas where UV light can activate surface-bound TiO_2. Notably, the gyroid structure, which showed the highest photocatalytic performance, has the highest number of printed layers (242), compared to 185 for the wheel and 171 for the lattice. The higher layer count increases the total intralayer surface area, providing more favourable sites for TiO_2 accumulation and thus promoting enhanced light–nanoparticles interactions during UV exposure. In addition to intralayer accumulation, localized enrichment of TiO_2 was consistently observed in structurally complex or intersecting regions across all geometries, such as the inner corner of the wheel (Fig. 6b"), the internal cavities of the gyroid (Fig. 6c"), and the interstitial zones of the lattice structure (Fig. 6d"). These non-uniform distributions, particularly the tendency of nanoparticles to accumulate in geometrically intricate or topologically constrained regions, lead to a higher local density of exposed active sites, resulting in variations in photocatalytic performance across different structures. Consistent with this interpretation, the lattice structure, although composed of a similar number of layers as the wheel (171 and 185, respectively), showed superior photocatalytic activity due to its elevated number of interstitial spaces, which enhance the nanoparticle surface enrichment.

Quantitative EDX elemental mapping of several regions of the printed samples further confirmed these trends (Fig. 7). In all systems, the surface TiO_2 content exceeds the bulk nanoparticle concentration determined by TGA analysis (Fig. 3b), supporting the tendency of the nanoparticles to migrate toward the surface during printing. Moreover, the surface TiO_2 concentration varied depending on the specific zone analysed. Geometrically simpler areas, such as the lateral surface of the wheel (region W3 in Fig. 7c), show lower TiO_2 content, whereas more complex regions, such as those in the spherical lattice structure (Fig. 7b), exhibit higher nanoparticle accumulation. The gyroid consistently displays the highest surface TiO_2 levels (Fig. 7a), suggesting that the increased architectural complexity of TPMS-based systems promotes more efficient nanoparticle migration toward the surface. This phenomenon can be theoretically framed within the segregation models for suspension-based additive manufacturing, as described by Bae et al. [51]. The non-uniform distribution is driven by the squeeze flow dynamics occurring during the platform's downward movement and the subsequent resin displacement. In complex architectures like the gyroid, the restricted flow paths and the significantly higher number of printing layers act as a 'geometrical trap' that promotes the accumulation of TiO_2 at the intralayer interfaces. As supported by Guillaume et al. [49], these interfaces often exhibit a higher filler concentration than the bulk due to the preferential migration of nanoparticles toward the liquid–solid

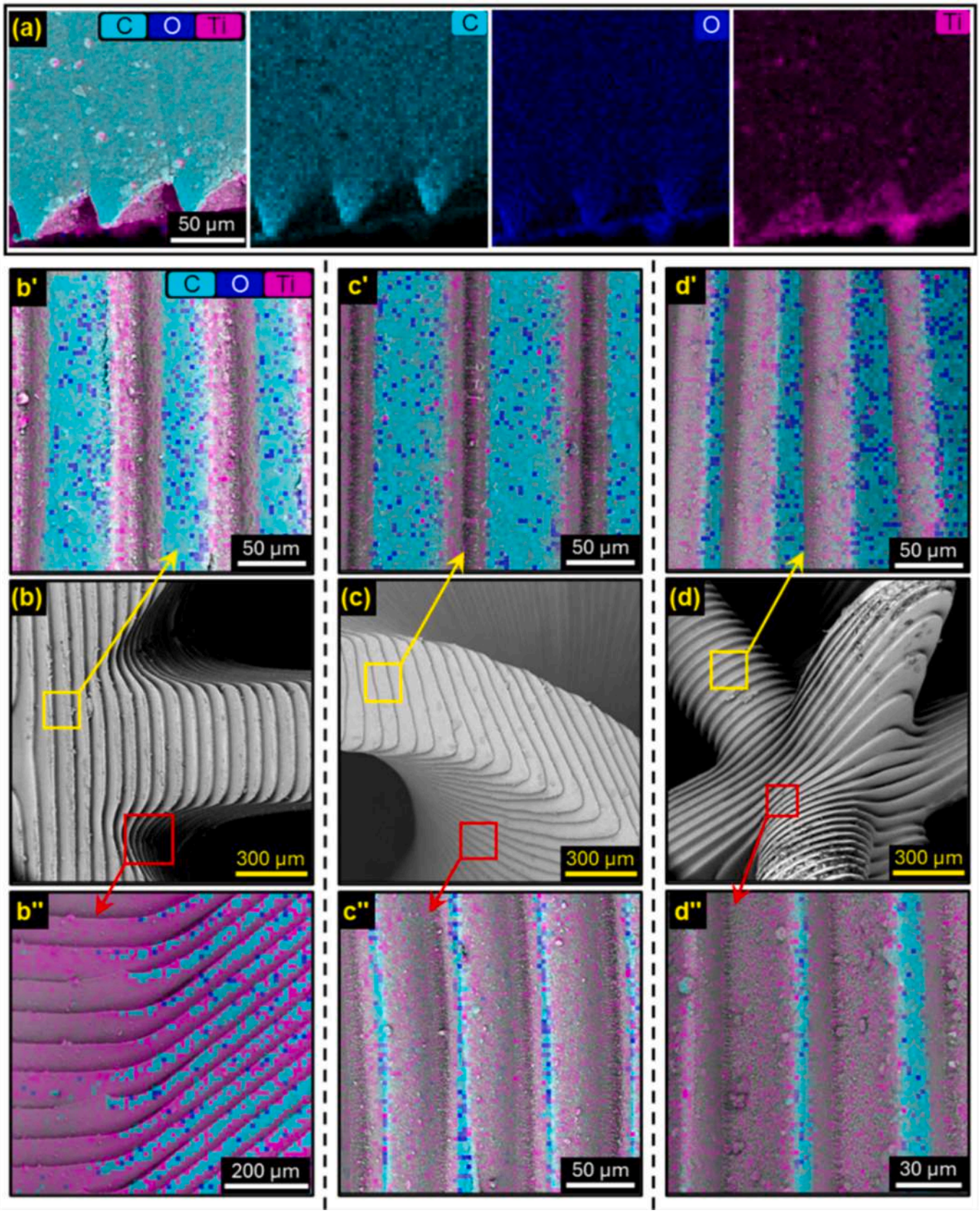

Fig. 6. Distribution of titanium dioxide on the surface of the three different printed samples. (a) EDX elemental mapping of C, O, and Ti in the cross-section of the wheel loaded with 10 wt% TiO_2; (b–d) SEM images and (b'–d', b''–d'') EDX elemental mapping of C, O, and Ti for the wheel (b, b', b''), gyroid (c, c', c''), and lattice (d, d', d'') structures loaded with 10 wt% TiO_2.

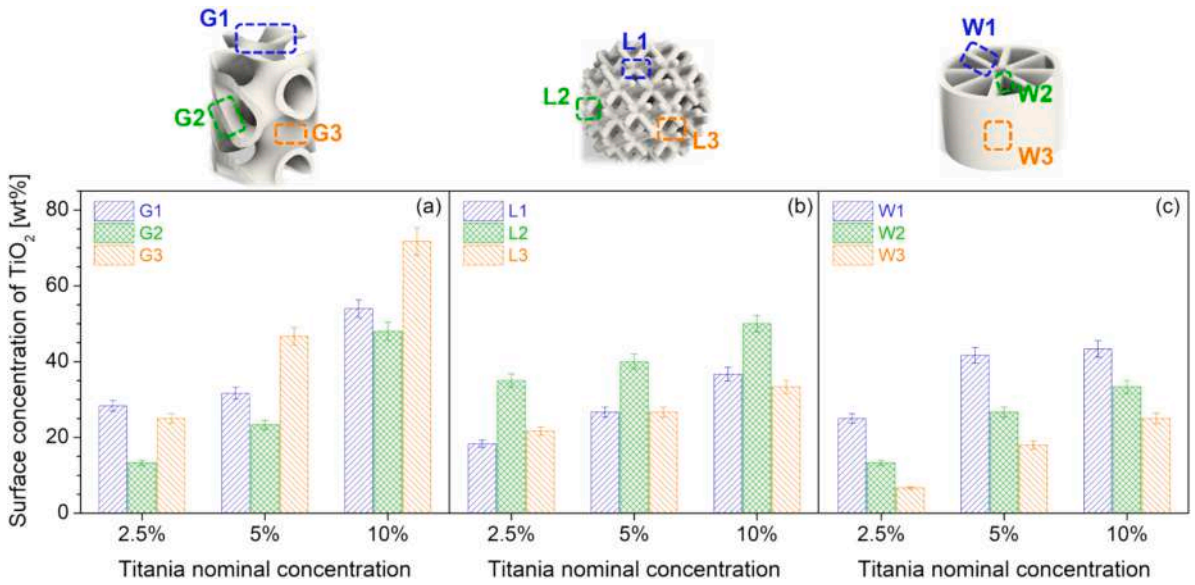

Fig. 7. Surface concentration of titanium dioxide measured by EDX elemental mapping in different regions of the printed samples at varying TiO_2 contents: (a) gyroid; (b) lattice; and (c) wheel.

boundary during the fast photopolymerization cycles. In summary, both geometric complexity and layer count play crucial roles in influencing nanoparticle localization within the printed structures. This, in turn, governs the availability of active TiO_2 sites, underscoring the importance of architectural design in optimizing the photocatalytic performance of LCD 3D-printed nanocomposites. It is worth noting that the observed trends in nanoparticle surface segregation and photocatalytic efficiency are specific to the studied resin–TiO_2 system processed by LCD vat photopolymerization. Changes in resin chemistry or formulation may affect light penetration, curing behavior, and nanoparticle migration during printing. Consequently, while the absolute photocatalytic performance may differ for other resin systems, the role of geometry and layer-by-layer fabrication in influencing nanoparticle distribution can still be considered a relevant design aspect for similar vat-photopolymerized composites.

4. Conclusions

The printability of TiO_2-based nanocomposites via LCD 3D printing, as well as the interplay between material formulation, processing parameters, and structural design in driving photocatalytic performance, were investigated. The incorporation of TiO_2 nanoparticles in a photocurable resin significantly affected photopolymerization kinetics by reducing cure depth due to enhanced UV light absorption and scattering. However, by optimizing exposure times for each formulation, accurate and high-resolution structures were successfully printed. Chemical, thermal, and morphological characterization confirmed the quality and integrity of the printed nanocomposites. ATR-FTIR analysis confirmed complete polymerization and the absence of residual monomers, while TGA and SEM/EDX analyses validated the thermal stability and effective dispersion of TiO_2 within the printed matrices. Notably, EDX mapping revealed a preferential accumulation of TiO_2 within intralayer and topologically complex regions, which play a central role in nanoparticle-light interactions and the consequent enhancement of photocatalytic efficiency. Photocatalytic performance, evaluated through methylene blue degradation as a model dye, was found to depend strongly on both TiO_2 concentration and printed geometry. Three geometries, wheel, lattice, and gyroid, were designed with identical nominal surface areas. Among the tested architectures, the gyroid structure exhibited the highest photocatalytic efficiency, attributed to its greater geometric complexity and higher number of layers, which promote more effective nanoparticle surface enrichment and UV activation. Overall, these findings highlight how structural design is essential for improving functional properties. By strategically tuning material formulation and geometry, it is possible to fabricate advanced 3D-printed devices for environmental remediation. Such applications include water and air purification, self-cleaning surfaces, and other technologies requiring light-activated catalytic functionality.

Funding

This research was funded by the European Union (NextGeneration EU) through the National Recovery and Resilience Plan (PNRR) project SAMOTHRACE – Sicilian MicronanoTech Research and Innovation Center (ECS00000022, CUP B63C22000620005) and by the Projects of Relevant National Interest (PRIN) 2022 PNRR project CO_2@photothermocat – Removal of air pollutants and valorization of the produced CO_2: hybrid catalysis to solve two issues at single blow (P2022JXKKF, CUP E53D23015700001).

Declaration of competing interest

The authors declare that they have no known competing financial interests or personal relationships that could have appeared to influence the work reported in this paper.

Appendix A. Supplementary data

Supplementary data to this article can be found online at https://doi.org/10.1016/j.matdes.2026.115639.

Data availability

Data will be made available on request.

References

[1] B. Mekuye, B. Abera, Nanomaterials: an overview of synthesis, classification, characterization, and applications, Nano Select 4 (2023) 486–501, https://doi.org/10.1002/nano.202300038.
[2] N. Baig, I. Kammakakam, W. Falath, Nanomaterials: a review of synthesis methods, properties, recent progress, and challenges, Mater. Adv. 2 (2021) 1821–1871, https://doi.org/10.1039/D0MA00807A.

[3] L.A. Kolahalam, I.V. Kasi Viswanath, B.S. Diwakar, B. Govindh, V. Reddy, Y.L. N. Murthy, Review on nanomaterials: Synthesis and applications, Mater. Today Proc. 18 (2019) 2182–2190, https://doi.org/10.1016/j.matpr.2019.07.371.

[4] M.M. El-Kady, I. Ansari, C. Arora, N. Rai, S. Soni, D.K. Verma, P. Singh, A. El Din Mahmoud, Nanomaterials: a comprehensive review of applications, toxicity, impact, and fate to environment, J. Mol. Liq. 370 (2023) 121046, https://doi.org/10.1016/j.molliq.2022.121046.

[5] S. Zahmatkesh, M. Hajiaghaei-Keshteli, A. Bokhari, S. Sundaramurthy, B. Panneerselvam, Y. Rezakhani, Wastewater treatment with nanomaterials for the future: a state-of-the-art review, Environ. Res. 216 (2023) 114652, https://doi.org/10.1016/j.envres.2022.114652.

[6] X. Chen, S.S. Mao, Titanium dioxide nanomaterials: synthesis, properties, modifications, and applications, Chem. Rev. 107 (2007) 2891–2959, https://doi.org/10.1021/cr0500535.

[7] S. Ji, C. Ye, Synthesis, growth mechanism, and applications of zinc oxide nanomaterials, J. Mater. Sci. Technol. 24 (2008) 457–473.

[8] S.J. Armaković, M.M. Savanović, S. Armaković, Titanium dioxide as the most used photocatalyst for water purification: an overview, Catalysts 13 (2022) 26–55, https://doi.org/10.3390/catal13010026.

[9] S. Peiris, H.B. De Silva, K.N. Ranasinghe, S.V. Bandara, I.R. Perera, Recent development and future prospects of TiO2 photocatalysis, J. Chinese Chemical Soc. 68 (2021) 738–769, https://doi.org/10.1002/jccs.202000465.

[10] N.M. Chauke, A. Ngqalakwezi, M. Raphulu, Transformative advancements in visible-light-activated titanium dioxide for industrial wastewater remediation, Int. J. Environ. Sci. Technol. 22 (2025) 8521–8552, https://doi.org/10.1007/s13762-025-06397-2.

[11] H.A. Colorado, E.I. Gutierrez-Velasquez, L.D. Gil, I.L. De Camargo, Exploring the advantages and applications of nanocomposites produced via vat photopolymerization in additive manufacturing: a review, Adv. Compos. Hybrid Mater. 7 (2024) 1–19, https://doi.org/10.1007/s42114-023-00808-z.

[12] Y. Zhu, Y. He, Y. Li, C. Liu, W. Lin, Heterogeneous porous synergistic photocatalysts for organic transformations, Chem Eur J 30 (2024) 202400842, https://doi.org/10.1002/chem.202400842.

[13] E. Lufrano, G. Curcuruto, M. Zimbone, A.A. Leonardi, G. Sfuncia, G. Nicotra, V. Strano, M.A. Buccheri, C. Simari, S.C. Carroccio, G. Impellizzeri, Contact Lenses–TiO_2 nanocomposites for a sustainable wastewater remediation, ACS Appl. Nano Mater. 8 (2024) 147–156, https://doi.org/10.1021/acsanm.4c05262.

[14] V. Spanò, M. Cantarella, M. Zimbone, F. Giuffrida, G. Sfuncia, G. Nicotra, A. Alberti, S. Scalese, L. Vitiello, S.C. Carroccio, G. Impellizzeri, TiO2—MoS2—PMMA nanocomposites for an efficient water remediation, Polymers 16 (2024) 1200, https://doi.org/10.3390/polym16091200.

[15] S. Alipoori, H. Rouhi, E. Linn, H. Stumpfl, H. Mokarizadeh, M.R. Esfahani, A. Koh, S.T. Weinman, E.K. Wujcik, Polymer-based devices and remediation strategies for emerging contaminants in water, ACS Appl. Polym. Mater. 3 (2021) 549–577, https://doi.org/10.1021/acsapm.0c01171.

[16] S. Sikiru, Y.O. Busari, J.O. Olutoki, M.M. Mahat, S.Y. Kolawole, Recent advances in polymer-based photocatalysts for environmental remediation and energy conversion: a review, J. Polym. Mater. 42 (2025) 1–31. https://doi.org/10.32604/jpm.2025.058936.

[17] V.T. Huong, B. Van Duc, N.T. An, T.T.P. Anh, T.M. Aminabhavi, Y. Vasseghian, S. W. Joo, 3D-printed WO3-UiO-66@reduced graphene oxide nanocomposites for photocatalytic degradation of sulfamethoxazole, Chem. Eng. J. 483 (2024) 149277, https://doi.org/10.1016/j.cej.2024.149277.

[18] A.O. Yusuf, S. Al Jitan, R. Al Sakkaf, H.S. Jarusheh, C. Garlisi, L.F. Dumée, G. Palmisano, 3D Printing to enable photocatalytic process engineering: A critical assessment and perspective, Appl. Mater. Today 35 (2023) 101940. https://doi.org/10.1016/j.apmt.2023.101940.

[19] B. Kaur, P. Singh, S. Thakur, A. Singh, V. Chaudhary, N. Kumar, A.A.P. Khan, M. A. Rub, N. Azum, P. Raizada, Harnessing 3D printing for tailored TiO_2 structures redefining organic pollutant degradation, J. Environ. Chem. Eng. 13 (2025) 116042, https://doi.org/10.1016/j.jece.2025.116042.

[20] C.H. Chen, S.C. Wang, H.W. Chen, T.Y. Chou, C.S. Chang, High-efficiency photocatalytic reactors fabricated via rapid DLP 3D Printing: enhanced dye photodegradation with optimized TiO_2 loading and structural design, ACS EST Water 4 (2024) 1883–1893, https://doi.org/10.1021/acsestwater.4c00002.

[21] N. Li, K. Tong, L. Yang, X. Du, Review of 3D printing in photocatalytic substrates and catalysts, Mater. Today Energy 29 (2022) 101100, https://doi.org/10.1016/j.mtener.2022.101100.

[22] K.R. Ryan, M.P. Down, N.J. Hurst, E.M. Keefe, C.E. Banks, Additive manufacturing (3D printing) of electrically conductive polymers and polymer nanocomposites and their applications, eScience 2 (2022) 365 – 381. https://doi.org/10.1016/j.esci.2022.07.003.

[23] H. Wu, W.P. Fahy, S. Kim, H. Kim, N. Zhao, L. Pilato, A. Kafi, S. Bateman, J.H. Koo, Recent developments in polymers/polymer nanocomposites for additive manufacturing, Prog. Mater Sci. 111 (2020) 100638, https://doi.org/10.1016/j.pmatsci.2020.100638.

[24] O. Abdulhameed, A. Al-Ahmari, W. Ameen, S.H. Mian, Additive manufacturing: challenges, trends, and applications, Adv. Mech. Eng. 11 (2019) 1687814018822880, https://doi.org/10.1177/1687814018822880.

[25] W.J. Chong, S. Shen, Y. Li, A. Trinchi, D. Pejak, I.L. Kyratzis, A. Sola, C. Wen, Additive manufacturing of antibacterial PLA-ZnO nanocomposites: Benefits, limitations and open challenges, J. Mater. Sci. Technol. 111 (2022) 120–151, https://doi.org/10.1016/j.jmst.2021.09.039.

[26] A. Al Rashid, S.A. Khan, S.G. Al-Ghamdi, M. Koç, Additive manufacturing of polymer nanocomposites: needs and challenges in materials, processes, and applications, J. Mater. Res. Technol. 14 (2021) 910–941, https://doi.org/10.1016/j.jmrt.2021.07.016.

[27] X. Zhou, J. Deng, C. Fang, W. Lei, Y. Song, Z. Zhang, Z. Huang, Y. Li, Additive manufacturing of CNTs/PLA composites and the correlation between microstructure and functional properties, J. Mater. Sci. Technol. 60 (2021) 27–34, https://doi.org/10.1016/j.jmst.2020.04.038.

[28] A.D. McQueen, M.L. Ballentine, L.R. May, C.H. Laber, A. Das, M.J. Bortner, A. J. Kennedy, Photocatalytic degradation of polycyclic aromatic hydrocarbons in water by 3D printed TiO_2 composites, ACS EST Water 2 (2021) 137–147, https://doi.org/10.1021/acsestwater.1c00299.

[29] A. Maurel, A.C. Martinez, S.B. Chavari, B. Yelamanchi, M.L. Seol, D.A. Dornbusch, W.H. Huddleston, S.T. Sreenivasan, C.G. Sherrard, E. MacDonald, 3D Printed TiO_2 negative electrodes for sodium-ion and lithium-ion batteries using vat photopolymerization, J. Electrochem. Soc. 170 (2023) 100538, https://doi.org/10.1149/1945-7111/ad0420.

[30] M. Shah, A. Ullah, K. Azher, A.U. Rehman, W. Juan, N. Aktürk, C. Sami Tufekci, M. U. Salamci, Vat photopolymerization-based 3D printing of polymer nanocomposites: current trends and applications, RSC Adv. 13 (2023) 1456–1496, https://doi.org/10.1039/D2RA06522C.

[31] Q. Li, Z. Pan, J. Liang, Z. Zhang, J. Li, Y. Zhou, X. Sun, Ceramic composites toughened by vat photopolymerization 3D printing technology, J. Mater. Sci. Technol. 146 (2023) 42–48, https://doi.org/10.1016/j.jmst.2022.10.035.

[32] H. Quan, T. Zhang, H. Xu, S. Luo, J. Nie, X. Zhu, Photo-curing 3D printing technique and its challenges, Bioact. Mater. 5 (2020) 110–115, https://doi.org/10.1016/j.bioactmat.2019.12.003.

[33] J.M. Aguirre-Cortes, A.I. Moral-Rodriguez, E. Bailon-Garcia, A. Davo-Quinonero, A. F. Perez-Cadenas, F. Carrasco-Marin, 3D printing in photocatalysis: Methods and capabilities for the improved performance, Appl. Mater. Today 32 (2023) 101831, https://doi.org/10.1016/j.apmt.2023.101831.

[34] N. Vidakis, D. Kalderis, M. Petousis, E. Maravelakis, N. Mountakis, N. Bolanakis, V. Papadakis, Biochar filler in MEX and VPP additive manufacturing: characterization and reinforcement effects in polylactic acid and standard grade resin matrices, Biochar 5 (2023) 39, https://doi.org/10.1007/s42773-023-00238-6.

[35] N. Vidakis, M. Petousis, E. Velidakis, A. Maniadim, Mechanical properties of 3D-printed ABS with combinations of two fillers: graphene nanoplatelets, TiO2, ATO nanocomposites, and zinc oxide micro (ZnOm), Recent Advances in Manufacturing Processes and Systems: Select Proceedings of RAM 2021, Springer Nature Singapore, Singapore, 2022, pp. 635-645. https://doi.org/10.1007/978-981-16-7787-8_51.

[36] N. Vidakis, M. Petousis, N. Michailidis, C. David, V. Saltas, D. Sagris, M. Spiridaki, A. Argyros, N. Mountakis, V. Papadakis, Interpretation of the optimization course of Silicon Nitride nano-powder content in biomedical resins for vat photopolymerization additive manufacturing, Ceram. Int. 50 (2024) 14919–14935, https://doi.org/10.1016/j.ceramint.2024.01.407.

[37] N. Vidakis, M. Petousis, A. Maniadi, V. Papadakis, A. Manousaki, MEX 3D printed HDPE/TiO_2 nanocomposites physical and mechanical properties investigation, J. Compos. Sci. 6 (2022) 209, https://doi.org/10.3390/jcs6070209.

[38] S. Dong, J. Feng, M. Fan, Y. Pi, L. Hu, X. Han, M. Lui, J. Sun, J. Sun, Recent developments in heterogeneous photocatalytic water treatment using visible light-responsive photocatalysts: a review, RSC Adv. 5 (2015) 14610–14630, https://doi.org/10.1039/C4RA13734E.

[39] K. Sonu, S.H. Puttaiah, V.S. Raghavan, S.S. Gorthi, Photocatalytic degradation of MB by TiO2: studies on recycle and reuse of photocatalyst and treated water for seed germination, Environ. Sci. Pollut. Res. 28 (2021) 48742–48753, https://doi.org/10.1007/s11356-021-13863-0.

[40] J. Bennett, Measuring UV curing parameters of commercial photopolymers used in additive manufacturing, Addit. Manuf. 18 (2017) 203–212, https://doi.org/10.1016/j.addma.2017.10.009.

[41] R. Bernasconi, U. Belle, S. Brigatti, M.V. Diamanti, 3D printing of photocatalytic nanocomposites containing titania nanoparticles, Addit. Manuf. 79 (2024) 103916, https://doi.org/10.1016/j.addma.2023.103916.

[42] P.F. Jacobs, Fundamentals of stereolithography, in: Proceedings for the 1992 International Solid Freeform Fabrication Symposium, Austin, Texas, 1992.

[43] J. Wong, S. Wei, R. Meir, N. Sadaba, N.A. Ballinger, E.K. Harmon, X. Gao, G. Altin-Yavuzarslan, L.D. Pozzo, L.M. Campos, A. Nelson, Triplet Fusion Upconversion for photocuring 3D-Printed particle-reinforced composite networks, Adv. Mater. 35 (2023) 2207673, https://doi.org/10.1002/adma.202207673.

[44] K. Madhusudan Reddy, S.V. Manorama, A. Ramachandra Reddy, Bandgap studies on anatase titanium dioxide nanoparticles, Mater. Chem. Phys. 78 (2003) 239–245, https://doi.org/10.1016/S0254-0584(02)00343-7.

[45] M. Madžarević, S. Ibrić, Evaluation of exposure time and visible light irradiation in LCD 3D printing of ibuprofen extended release tablets, Eur. J. Pharm. Sci. 158 (2021) 105688, https://doi.org/10.1016/j.ejps.2020.105688.

[46] Y. Liu, J.H. Campbell, O. Stein, L. Jiang, J. Hund, Y. Lu, Deformation behavior of foam laser targets fabricated by two-photon polymerization, Nanomaterials 8 (2018) 498, https://doi.org/10.3390/nano8070498.

[47] C. Sriwong, K. Choojun, S. Sriwong, High photocatalytic performance of 3D porous-structured TiO2@natural rubber hybrid sheet on the removal of indigo carmine dye in water, SN Appl. Sci. 1 (2019) 864, https://doi.org/10.1007/s42452-019-0900-y.

[48] P.J. Bártolo, Stereolithography: materials, processes and applications, Springer Science & Business Media, 2011.

[49] O. Guillaume, M.A. Geven, C.M. Sprecher, V.A. Stadelmann, D.W. Grijpma, T. T. Tang, L. Qin, Y. Lai, M. Alini, J.D. De Bruijn, H. Yuan, R.G. Richards, D. Eglin, Surface-enrichment with hydroxyapatite nanoparticles in stereolithography-

fabricated composite polymer scaffolds promotes bone repair, Acta Biomater. 54 (2017) 386–398, https://doi.org/10.1016/j.actbio.2017.03.006.
[50] U. Bellè, F. Pelizzari, A. Lucotti, C. Castiglioni, M. Ormellese, M. Pedeferri, M. V. Diamanti, Immobilized Nano-TiO_2 photocatalysts for the degradation of three organic dyes in single and multi-dye solutions, Coatings 10 (2020) 919, https://doi.org/10.3390/coatings10100919.
[51] C.J. Bae, J.W. Halloran, Segregation model study of suspension-based additive manufacturing, J. Eur. Ceram. Soc. 38 (2018) 5160–5166, https://doi.org/10.1016/j.jeurceramsoc.2018.07.008.